QUANTUM ELECTRONICS

Measurement of a superconducting qubit with a microwave photon counter

A. Opremcak^{1*}, I. V. Pechenezhskiy^{1*}†, C. Howington², B. G. Christensen¹, M. A. Beck¹, E. Leonard Jr.¹, J. Suttle¹, C. Wilen¹, K. N. Nesterov¹, G. J. Ribeill¹‡, T. Thorbeck¹§, F. Schlenker¹, M. G. Vavilov¹, B. L. T. Plourde², R. McDermott¹||

Fast, high-fidelity measurement is a key ingredient for quantum error correction. Conventional approaches to the measurement of superconducting qubits, involving linear amplification of a microwave probe tone followed by heterodyne detection at room temperature, do not scale well to large system sizes. We introduce an approach to measurement based on a microwave photon counter demonstrating raw single-shot measurement fidelity of 92%. Moreover, the intrinsic damping of the photon counter is used to extract the energy released by the measurement process, allowing repeated high-fidelity quantum nondemolition measurements. Our scheme provides access to the classical outcome of projective quantum measurement at the millikelvin stage and could form the basis for a scalable quantum-to-classical interface.

o harness the tremendous potential of quantum computers, it is necessary to implement robust error correction to combat decoherence of the fragile quantum states. Error correction relies on high-fidelity, repeated measurements of an appreciable fraction of the quantum array throughout the run time of the algorithm (1). In the context of superconducting qubits, measurement is performed by heterodyne detection of a weak microwave probe tone transmitted across or reflected from a linear cavity that is dispersively coupled to the qubit (2-8). This approach relies on bulky, magnetic nonreciprocal circuit components to isolate the qubit from noisy amplification stages (5, 9-11); moreover, the measurement result is only accessible after room-temperature heterodyne detection and thresholding, complicating efforts to implement low-latency feedback conditioned on the measurement result (12, 13). The physical footprint, wiring heat load, and latency associated with conventional amplifier-based qubit measurement stand as major impediments to scaling superconducting qubit technology.

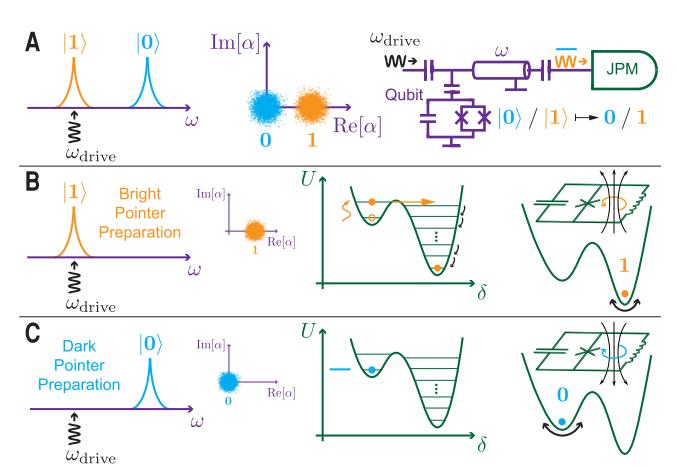
An alternative approach involves entanglement of the qubit with the linear resonator to create cavity pointer states characterized by large differential photon occupation, followed by subsequent photodetection (14). In our experiments (Fig. 1A), microwave drive at one of the two dressed cavity frequencies maps the qubit state onto "bright" and "dark" cavity pointer states. Discrimination of the states is performed directly

||Corresponding author. Email: rfmcdermott@wisc.edu

at the millikelvin stage by the Josephson photomultiplier (JPM), a microwave photon counter; we use no nonreciprocal components between the qubit and JPM. The JPM is based on a single Josephson junction in a radiofrequency superconducting quantum interference device (SQUID) loop that is biased close to the critical flux where a phase slip occurs. The circuit parameters are chosen to yield a potential energy landscape with one or two local minima, depending on flux bias; the distinct local minima correspond to classically distinguishable flux states in the device [see (15), section S1]. Once the JPM is properly biased, the presence of resonant microwaves induces a rapid tunneling event between the two classically distinguishable states of the detector (Fig. 1B). In the absence of microwave input, transitions

Fig. 1. Qubit state measurement using the

JPM. (A) Measurement overview. Microwave drive at the dressed cavity resonance corresponding to the qubit |1⟩ state creates bright and dark cavity pointer states with large differential photon occupation. These pointer states are detected using the JPM, which stores the measurement result as a classical bit at the millikelvin stage. (B) Bright pointer detection. Micro-



waves resonant with the JPM promote the circuit from the ground state of a metastable local minimum (here, left potential well) to an excited state. The detector subsequently undergoes a rapid tunneling transition that allows relaxation to the global minimum of the potential (here, right potential well). (\mathbf{C}) Dark pointer detection. Energy contained in the dark pointer state is insufficient to induce a tunneling event. The presence (B) or absence (C) of an interwell tunneling transition results in classically distinguishable flux (oscillation) states in the detector.

occur at an exponentially suppressed dark rate (Fig. 1C). Thus, the absorption of resonant microwaves creates a readily measured "click" (16).

The qubit and the JPM are fabricated on different silicon substrates and housed in separate aluminum enclosures connected via a coaxial transmission line with characteristic impedance $Z_0=50~\Omega$ and length $L_0=14~\mathrm{cm}$ [see (15), sections S2 and S3]. The qubit chip (purple circuit in Fig. 2A) incorporates an asymmetric transmon (Fig. 2B) that is capacitively coupled to a half-wave coplanar waveguide (CPW) resonator, the qubit cavity, with frequency $\omega_1/2\pi=5.020~\mathrm{GHz}$ and qubit-cavity coupling strength $g_1/2\pi=110~\mathrm{MHz}$ (17–19). The qubit is operated at a fixed frequency $\omega_q/2\pi=4.433~\mathrm{GHz}$ and has an anharmonicity $\alpha/2\pi=-250~\mathrm{MHz}$.

The JPM (green circuit in Fig. 2A) is based on the capacitively shunted flux-biased phase qubit (20). The JPM is capacitively coupled to a local auxiliary CPW resonator, the capture cavity, with bare frequency $\omega_2/2\pi$ = 5.028 GHz and coupling strength $g_2/2\pi = 40$ MHz. A micrograph of the JPM is shown in Fig. 2C. The circuit involves a single Al-AlO_x-Al Josephson junction with critical current $I_0 = 1 \mu A$ embedded in a 3+3 turn gradiometric loop with inductance L_g = 1.1 nH. The junction is shunted by an external parallel-plate capacitor $C_s = 3.3$ pF. The plasma frequency of the JPM is tunable with external flux from 5.9 to 4.4 GHz (Fig. 2, D and E), allowing for both resonant and dispersive interactions between the JPM and capture cavity.

The qubit and capture cavities are capacitively coupled to the mediating transmission line [see also (15), section S4 and tables S1 to S3]. After pointer state preparation, microwave energy leaks out of the qubit cavity, and a fraction of that energy is transferred to the capture cavity (21). Without an intervening isolator or circulator to damp unwanted reflections, the finite length L_0 of the transmission line admits a standing wave structure with an approximate mode spacing of

¹Department of Physics, University of Wisconsin–Madison, Madison, WI 53706, USA. ²Department of Physics, Syracuse University, Syracuse, NY 13244, USA.

^{*}These authors contributed equally to this work. †Present address: University of Maryland, College Park, MD 20742, USA. ‡Present address: Raytheon BBN Technologies, Cambridge, MA 02138, USA. §Present address: IBM T. J. Watson Research Center, Yorktown Heights, NY 10598, USA.

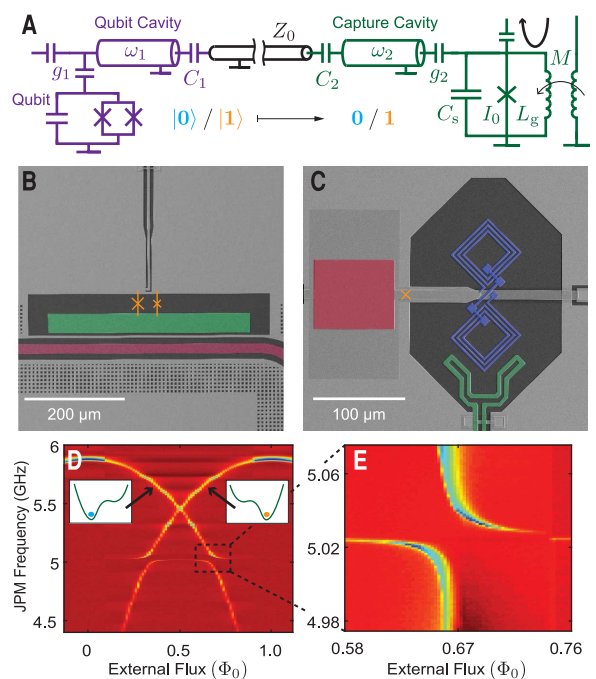
 $v_p/2L_0$, where v_p is the phase velocity of propagation in the cable. With these complications in mind, L_0 was chosen to avoid destructive interference in the vicinity of ω_1 and ω_2 , which can substantially degrade photon transfer efficiency [see (15), section S5].

In the timing diagram of the measurement (Fig. 3A), the cartoon insets depict the dynamics of the JPM phase particle at critical points throughout the measurement sequence. We begin with a deterministic reset of the JPM, which is accomplished by biasing the JPM potential into a single-well configuration [see (15), section S1]. A depletion interaction between the JPM and capture cavity mode immediately follows in order to dissipate spurious microwave excitations generated during reset. Additional details of this depletion process are described below and in Fig. 4, A and B. Next, we use mode repulsion between the JPM and capture cavity to tune ω_2 in order to maximize photon transfer efficiency. The response of the capture cavity to an applied drive tone at four distinct JPM-capture cavity detunings, and thus four different values of ω_2 , is shown in Fig. 3B; the detuning is chosen such that ω_1 = ω_2 . At the beginning of the tune and capture stage, a qubit X-gate (I-gate) is performed and a subsequent qubit cavity drive tone is applied to prepare the bright (dark) pointer state [see (15), section S6]. The cavities are held on resonance for 750 ns to allow the pointer states to leak from the qubit cavity to the capture cavity; this time was determined by maximizing measurement fidelity with respect to the drive pulse duration. The bright pointer state corresponds to a mean qubit cavity photon occupation $\bar{n}_1 \sim 10$, calibrated using the ac Stark effect (Fig. 3E) [see (15), section S8] (22, 23). After pointer state transfer, the JPM is biased into resonance with the capture cavity, and occupation of that mode induces intrawell excitations of the phase particle on a time scale $\pi/2g_2 \sim 6$ ns (Fig. 3C) (24). Finally, a short (~10 ns) bias pulse is applied to the JPM to induce interwell tunneling of excited states (25); the amplitude of the bias pulse is adjusted to maximize tunneling contrast between qubit excited and ground states (Fig. 3D). At this point, the measurement is complete: The measurement result is stored in the classical flux state of the JPM. To retrieve the result of qubit measurement for subsequent analysis at room temperature, we use a weak microwave probe tone to interrogate the plasma resonance of the JPM after measurement. The JPM bias is adjusted so that the plasma frequencies associated with the two local minima in the potential are slightly different; reflection from the JPM can distinguish the flux state of the detector with >99.9% fidelity in <500 ns [see (15), section S4].

Each measurement cycle yields a binary result -"0" or "1"-the classical result of projective quantum measurement. To access qubit state occupation probabilities, the measurement is repeated 10,000 times. The JPM switching probabilities represent raw measurement outcomes, uncorrected for state preparation, relaxation, or gate errors. In Fig. 3, F and G, we display the raw

Fig. 2. Experimental setup.

(A) Circuit schematic. The qubit circuit (purple) is connected to the JPM circuit (green) via a coaxial transmission line (black) [see (15), tables S1 to S3]. (B) Micrograph of the transmon circuit with superconducting island (green), qubit cavity (maroon), and Josephson junctions (orange). (C) Micrograph of the JPM circuit (capture cavity not shown) with its 3+3 turn gradiometric loop inductance Lg (blue), single Josephson junction with critical current I_0 (orange), parallel-plate capacitor C_s (red), and on-chip flux bias line with mutual inductance M (green). (**D**) JPM spectroscopy versus external flux. Insets show cartoons of a phase particle bound to the left and right wells. (E) Enlargement of the avoided level crossing between the JPM and capture cavity.



measurement outcomes for qubit Ramsey and Rabi experiments, respectively. The JPM measurements achieve a raw fidelity of 92%. The bulk of our fidelity loss is due to qubit energy relaxation during pointer state preparation and dark counts, which contribute infidelity of 5% and 2%, respectively. In our setup, dark counts stem from both excess |1| population of the qubit and spurious microwave energy contained in our dark pointer state. We attribute the remaining infidelity to imperfect gating and photon loss during pointer state transfer. The qubit T_1 of 6.6 μ s measured in these experiments is consistent with separate measurements of the same device using conventional heterodyne readout techniques; we see no evidence of JPM-induced degradation of qubit T_1 .

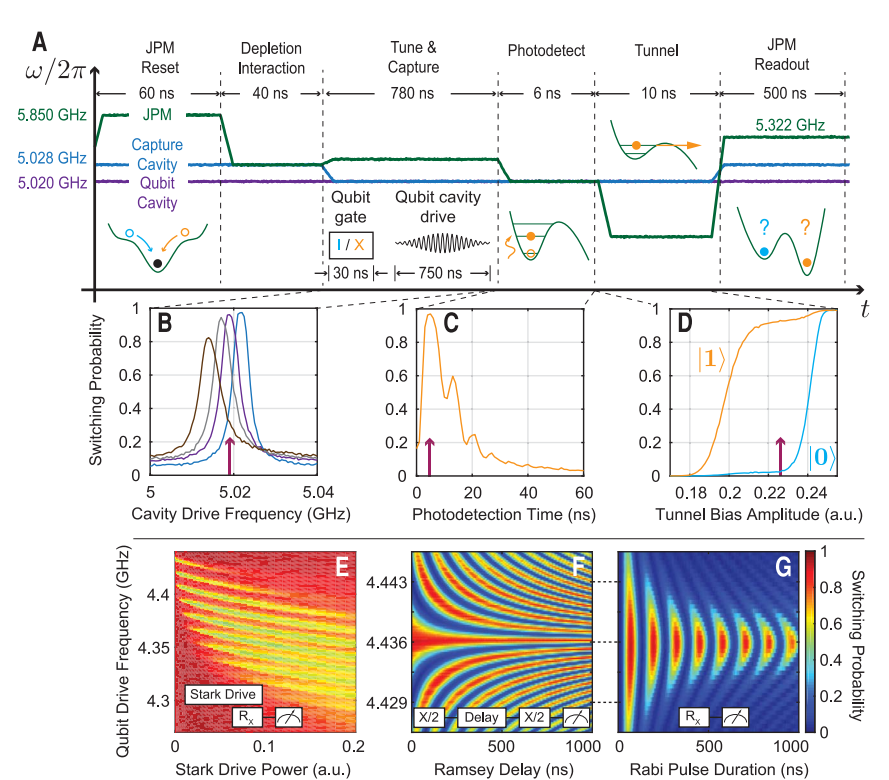
As noted earlier, JPM switching events release a large energy on the order of 100 photons as the JPM relaxes from a metastable minimum to the global minimum of its potential (26). It is critical to understand the backaction of JPM switching events on the qubit state. The JPM tunneling transient has a broad spectral content, and Fourier components of this transient that are resonant with the capture and qubit cavities will induce a spurious population in these modes that will lead to photon shot noise dephasing of the qubit (27, 28). In Fig. 4A, we show the results of qubit Ramsey scans performed with (orange) and without (blue) a forced JPM tunneling event before the experiment. In the absence of any mitigation of the classical backaction, qubit Ramsey fringes show strongly suppressed coherence and a frequency shift indicating spurious photon occupation in the qubit cavity (29). However, we can use the intrinsic damping of the JPM mode itself to controllably dissipate the energy in the linear cavities and fully suppress photon shot noise dephasing. Immediately after JPM reset, the JPM is biased to a point where the levels in the shallow minimum are resonant with the linear cavity modes. Energy from the capture cavity leaks back to the JPM, inducing intrawell transitions; at the selected bias point, the interwell transition probability is negligible. The JPM mode is strongly damped, with quality factor $Q \sim 300$, set by the loss tangent of the SiO2 dielectric used in the JPM shunt capacitor (30). As a result, the energy coupled to the JPM is rapidly dissipated. With this deterministic reset of the cavities, fully coherent qubit Ramsey fringes that correspond to the absence of a JPM switching event are recovered for depletion times ≥40 ns, as shown in Fig. 4B. We reiterate that no nonreciprocal components are used in these experiments to isolate the qubit chip from the classical backaction of the JPM.

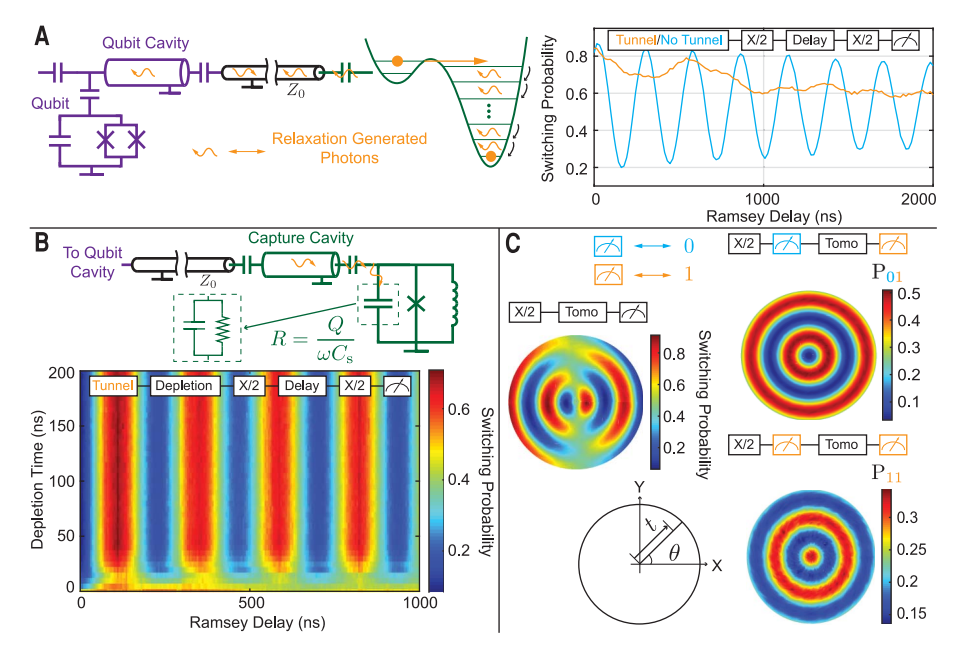
In Fig. 4C we explore the quantum nondemolition (QND) character of our measurement protocol (31). We prepare the qubit in the superposition state $(|0\rangle - i|1\rangle/\sqrt{2})$ aligned along the -y axis of the Bloch sphere. We verify the state by performing an overdetermined tomography (20). Here the direction θ and length t of a tomographic pulse are swept continuously over the equatorial plane of the Bloch sphere before measurement. For control pulses applied along the x axis, the qubit undergoes the usual Rabi oscillations; for control applied along y, the qubit state vector is unaffected. After an initial JPMbased measurement (including an additional 1.4 µs of delay for qubit cavity ringdown), we perform a tomographic reconstruction of the qubit state by applying a prerotation and a final JPM-based measurement. In the right-hand panel of Fig. 4C, we display tomograms corresponding to the classical measurement results "0" (top) and "1" (bottom). When the measurement result "0" is returned, we find a tomogram that

Fig. 3. JPM-based qubit measurement. (A) We begin by resetting the JPM into a well-defined flux state. A subsequent depletion interaction removes spurious microwave excitations generated during reset (see Fig. 4, A and B, for more details). (B) Next, we tune the capture cavity frequency to maximize transfer efficiency from the qubit cavity. The response of the capture cavity to an applied drive at four distinct JPM-capture cavity detunings is shown; the detuning is chosen such that $\omega_2 = \omega_1$. During the tune and capture interval, a qubit X-gate (I-gate) is applied, and microwave drive at the dressed |1| cavity resonance is used to prepare the bright (dark) pointer state. As we drive the qubit cavity, a fraction of the microwave energy is transferred to the capture cavity during this capture step. (C) The JPM is then tuned into resonance with the capture cavity for photodetection. Photons present in the capture cavity induce intrawell transitions of the JPM to higher excited states. (**D**) Finally, a brief bias pulse is applied to induce tunneling of excited JPM states. The arrows on the bottom axes in (B) to (D) indicate optimal bias parameters. At this point, the measurement is complete, and the result is encoded in the classical flux state of the JPM. Microwave reflectometry is subsequently used to interrogate the JPM. (E) Stark spectroscopy used to calibrate qubit cavity photon occupation. JPM-detected Ramsey fringes and Rabi oscillations versus qubit drive detuning are shown in (F) and (G), respectively.

Fig. 4. Mitigating backaction and preserving QND properties. (A) The JPM switching event releases energy on the order of 100 photons, inducing spurious population of the capture and qubit cavities. The right-hand panel shows baseline qubit Ramsey fringes (blue) and Ramsey fringes measured after a forced tunneling event by the JPM (orange). (B) After the fast flux pulse that induces JPM tunneling, we adjust JPM bias so that energy deposited in the cavities is dissipated in the JPM, yielding a deterministic reset of the cavities. The color plot shows qubit Ramsey fringes versus duration of the depletion interaction between the JPM and the capture cavity. (C) Qubit tomography after JPM-based measurement. We prepare the superposition state $(|0\rangle - i|1\rangle/\sqrt{2})$ and verify the state with overdetermined qubit tomography (left panel). To characterize the qubit state after JPM-based measurement, we prepare the same superposition state, measure with the JPM, and then perform qubit tomography on the resulting state. Qubit tomography conditioned on the JPM measurement shows high overlap with target states $|0\rangle$ (top right) and $|1\rangle$ (bottom right).

overlaps with the ideal $|0\rangle$ state with fidelity 91% [see (15), section S9]. When the result "1" is returned, the measured tomogram corresponds to overlap fidelity of 69% with the $|1\rangle$ state. The loss in fidelity for the qubit $|1\rangle$ state is consistent with the measured qubit T_1 time of 6.6 μ s and the 2.8 μ s between successive measurement drive tones. We conclude that our JPM-based measurement is highly QND.





Our high-fidelity, fast photon counter-based qubit measurement approach provides access to the binary result of projective quantum measurement at the millikelvin stage without the need for nonreciprocal components between the qubit and counter. In a future system, JPM-based readout could form the basis of the measurement side of a robust, scalable interface between a quantum array and a proximal classical controller, for

example, by encoding the flux state of the JPM onto classical single-flux quantum (SFQ) voltage pulses (32, 33) for subsequent postprocessing via SFQ-based digital logic (34).

REFERENCES AND NOTES

- A. G. Fowler, M. Mariantoni, J. M. Martinis, A. N. Cleland, *Phys. Rev. A* 86, 032324 (2012).
- A. Blais, R.-S. Huang, A. Wallraff, S. M. Girvin, R. J. Schoelkopf, Phys. Rev. A 69, 062320 (2004).

- 3. I. Siddiqi et al., Phys. Rev. Lett. 93, 207002 (2004).
- F. Mallet et al., Nat. Phys. 5, 791-795 (2009).
- E. Jeffrey et al., Phys. Rev. Lett. 112, 190504 (2014).
- 6. J. Kelly et al., Nature 519, 66-69 (2015).
- J. M. Martinis, npj Quantum Inf. 1, 15005 (2015).
- 8. D. Sank et al., Phys. Rev. Lett. 117, 190503 (2016).
- J. E. Johnson et al., Phys. Rev. Lett. 109, 050506 (2012).
- 10. C. Macklin et al., Science 350, 307-310 (2015).
- 11. T. Walter et al., Phys. Rev. Appl. 7, 054020 (2017).
- 12. D. Ristè, J. G. van Leeuwen, H.-S. Ku, K. W. Lehnert, L. DiCarlo, Phys. Rev. Lett. 109, 050507 (2012).
- 13. D. Ristè et al., Nature 502, 350-354 (2013).
- 14. L. C. G. Govia et al., Phys. Rev. A 90, 062307 (2014).
- 15. See supplementary materials.
- 16. Y.-F. Chen et al., Phys. Rev. Lett. 107, 217401 (2011).
- 17. J. Koch et al., Phys. Rev. A 76, 042319 (2007).
- 18. R. Barends et al., Phys. Rev. Lett. 111, 080502 (2013).
- 19. M. D. Hutchings et al., Phys. Rev. Appl. 8, 044003 (2017).
- 20. M. Steffen et al., Phys. Rev. Lett. 97, 050502 (2006).
- 21. J. Wenner et al., Phys. Rev. Lett. 112, 210501 (2014).
- 22. D. I. Schuster et al., Phys. Rev. Lett. 94, 123602 (2005).
- 23. D. I. Schuster et al., Nature 445, 515-518 (2007).
- 24. M. Hofheinz et al., Nature 454, 310-314 (2008).
- 25. K. B. Cooper et al., Phys. Rev. Lett. 93, 180401 (2004).
- 26. R. McDermott et al., Science 307, 1299-1302 (2005).
- 27. A. P. Sears et al., Phys. Rev. B 86, 180504 (2012).

- 28. F. Yan et al., Nat. Commun. 7, 12964 (2016).
- 29. D. T. McClure et al., Phys. Rev. Appl. 5, 011001 (2016).
- 30. J. M. Martinis et al., Phys. Rev. Lett. 95, 210503 (2005).
- 31. A. Lupaşcu, C. J. M. Verwijs, R. N. Schouten, C. J. P. M. Harmans, J. E. Mooij, Phys. Rev. Lett. 93, 177006 (2004).
- 32. A. Herr (Kidiyarova-Shevchenko), A. Fedorov, A. Shnirman, E. Il'ichev, G. Schön, Supercond. Sci. Technol. 20, S450-S454
- 33. K. G. Fedorov, A. V. Shcherbakova, M. J. Wolf, D. Beckmann, A. V. Ustinov, Phys. Rev. Lett. 112, 160502 (2014).
- 34. R. McDermott et al., Quantum Sci. and Technol. 3, 024004 (2018).

ACKNOWLEDGMENTS

We acknowledge stimulating discussions with M. Vinje, L. B. loffe, and M. Saffman. Portions of this work were performed in the Wisconsin Center for Applied Microelectronics, a research core facility managed by the College of Engineering and supported by the University of Wisconsin-Madison. Other portions were performed at the Cornell NanoScale Facility, a member of the National Nanotechnology Coordinated Infrastructure (NNCI), which is supported by the National Science Foundation under grant no. ECCS-1542081. R.M., B.L.T.P., and M.G.V. are inventors on patent number US 9,692,423 B2 held by Wisconsin Alumni Research Foundation, Syracuse University, and Universität des

Saarlandes that covers a system and method for circuit quantum electrodynamics measurement. **Funding:** This work was supported by the U.S. Government under ARO grants W911NF-14-1-0080 and W911NF-15-1-0248. Author contributions: R.M. and B.L.T.P. designed and oversaw the experiment. A.O. and C.H. designed and fabricated the samples. A.O., I.V.P., and B.G.C. performed the experiment and analyzed the data. B.G.C., M.G.V., and K.N.N. provided theoretical assistance. A.O., I.V.P., C.H., B.G.C., M.G.V., B.L.T.P., and R.M. co-wrote the manuscript. All remaining authors contributed to the experimental setup, software infrastructure, or fabrication recipes used in these experiments. Competing interests: The authors declare no competing financial interests. Data and materials availability: All data, materials, and unique computer codes necessary to understand and assess the conclusions of this paper are available in the supplementary materials.

SUPPLEMENTARY MATERIALS

www.sciencemag.org/content/361/6408/1239/suppl/DC1 Materials and Methods Figs. S1 to S6

Tables S1 to S3 References (35, 36)

28 February 2018: accepted 17 July 2018 10.1126/science.aat4625



Measurement of a superconducting qubit with a microwave photon counter

A. Opremcak, I. V. Pechenezhskiy, C. Howington, B. G. Christensen, M. A. Beck, E. Leonard Jr., J. Suttle, C. Wilen, K. N. Nesterov, G. J. Ribeill, T. Thorbeck, F. Schlenker, M. G. Vavilov, B. L. T. Plourde and R. McDermott

Science **361** (6408), 1239-1242. DOI: 10.1126/science.aat4625

Counting the state of a qubit

Operation of a quantum computer will be reliant on the ability to correct errors. This will typically require the fast, high-fidelity quantum nondemolition measurement of a large number of qubits. Opremcak et al. describe a method that uses a photon counter to determine the state of a superconducting qubit. Being able to simply read out the qubit state as a photon number removes the need for bulky components and large experimental overhead that characterizes present approaches.

Science, this issue p. 1239

ARTICLE TOOLS http://science.sciencemag.org/content/361/6408/1239

SUPPLEMENTARY MATERIALS http://science.sciencemag.org/content/suppl/2018/09/19/361.6408.1239.DC1

REFERENCES This article cites 35 articles, 2 of which you can access for free http://science.sciencemag.org/content/361/6408/1239#BIBL

PERMISSIONS http://www.sciencemag.org/help/reprints-and-permissions

Use of this article is subject to the Terms of Service